CLOSDI: A Novel Spectral Index for Cloud Shadow Detection in Sentinel-2 Imagery Using NDVI and EVI2

Adrián Cal

Instituto Nacional de Investigación Agropecuaria (INIA), Área de Sistemas de Información y Transformación Digital (GRAS), Estación Experimental INIA Las Brujas, Ruta 48 km 10, Rincón del Colorado, 90100, Canelones, Uruguay

ORCID: 0000-0002-2773-0471

e-mail: acal@inia.org.uy

This manuscript has been accepted for publication in Remote Sensing Applications: Society and Environment (2026).

ABSTRACT

Cloud shadows constitute a significant source of uncertainty in optical remote sensing, thereby impairing the accuracy of spectral indices, land cover classifications, and time-series analyses derived from Sentinel-2 imagery. Although the Sentinel-2 Level-2A Scene Classification Layer (SCL) offers information on cloud shadows, its efficacy is frequently hindered by high omission rates and inconsistent detection. This study presents a novel spectral index, namely, the Cloud Shadow Detection Index (CLOSDI), which is specifically designed to enhance cloud shadow detection within agricultural and grassland landscapes.

CLOSDI is derived from the differential sensitivity of the Normalized Difference Vegetation Index (NDVI) and the two-band Enhanced Vegetation Index (EVI2) to shadow conditions and can be computed directly from RED and NIR reflectance using a closed-form formulation. The index was evaluated using 1,231 high-quality image patches from the CloudSEN12 dataset, which are restricted to temperate and tropical grassland biomes. An optimal cutoff threshold of 34.0 was identified through an 80/20 training–testing split by maximizing the median intersection over union (IoU).

On the test set, CLOSDI substantially outperformed the Sentinel-2 SCL-based shadow mask. The median performance metrics were: recall of 76.8 versus 19.6, F1-score of 62.1 versus 19.6, IoU of 45.0 versus 16.7, and balanced overall accuracy of 80.1 versus 57.6 for CLOSDI and SCL, respectively. A Wilcoxon signed-rank test confirmed that the improvement in IoU was statistically significant ($p = 1.402 \times 10^{-19}$). Despite using only two spectral bands, CLOSDI achieved a performance comparable to state-of-the-art cloud shadow detection algorithms, while requiring substantially lower computational complexity and eliminating the need for model training.

These findings illustrate that the CLOSDI offers a straightforward, physically interpretable, and computationally efficient approach for cloud shadow detection within vegetation-dominated landscapes. Its ease of implementation and robust performance render it particularly appropriate for large-scale agricultural monitoring, vegetation time-series analysis, and operational remote sensing workflows.

Keywords: Cloud shadow detection, Sentinel-2, CLOSDI, CloudSEN12, Scene Classification Layer (SCL)

1. Introduction

The launch of the Sentinel-2A satellite in June 2015, followed by its twin satellites Sentinel-2B in 2017 and Sentinel-2C in 2024, has significantly advanced Earth observation capabilities.

As of February 2026, this mission resulted in over 200,000 scientific publications indexed in Google Scholar. The spectrum of Sentinel-2 applications is broad and encompasses research on

ice and glaciers, oceans and seas, rivers and lakes, soil and vegetation, air quality, floods, and wildfires (European Space Agency, n.d.).

The successful features of the mission include comprehensive global coverage, a spatial resolution of 10 m for visible and near-infrared (NIR) bands and up to 20 m for red-edge and short-wave infrared (SWIR) bands, a revisit frequency of five days, the acquisition of thirteen spectral bands (Copernicus SentiWiki, n.d.), the capacity to compute hundreds of spectral indices, such as those documented in the Awesome Earth Engine Spectral Indices library (Awesome Spectral Indices, n.d.), and its open and freely accessible nature. Furthermore, it can be integrated with other optical sensors, such as Landsat 8 (Claverie et al., 2018).

Notwithstanding its numerous strengths, Sentinel-2 exhibits an inherent limitation common to optical sensors: a significant proportion of its imagery contains pixels affected by clouds or cloud shadows, thereby compromising its applicability for various analytical purposes. To address this issue, the Level-2A product incorporates, in addition to spectral bands, a Scene Classification Layer (SCL). This layer assigns each pixel a land cover classification (e.g., vegetation, water, bare soil, cloud shadow, snow) and is generated by the Sen2Cor algorithm (Main-Knorn et al., 2017). The SCL band supports the filtering of unreliable pixels, such as clouds, shadows, saturated pixels, and no-data pixels, retaining only those suitable for analysis. However, numerous studies assessing the applicability of SCL for cloud shadow detection have identified several significant limitations. The primary issues include the frequent omission of actual shadows (false negatives), particularly over dark surfaces such as water bodies or dense vegetation; false positives, in which shadows are mistaken for water bodies or other dark regions; suboptimal performance in complex scenes featuring thin clouds or low illumination; and a pronounced dependence on the quality of cloud detection, as inaccuracies in cloud identification directly influence the placement of their shadows (Domnich et al., 2021; Layton et al., 2023; Li et al., 2022; Liang et al., 2024; Raiyani et al., 2021; Tarrio et al., 2020; Wright et al., 2024; Zekoll et al., 2022).

The presence of shadows considerably influences reflectance across all spectral bands, impacting the computation of indices such as SAVI or EVI and resulting in potential misinterpretations or erroneous outcomes in models or classifications. Given that shadows influence image analysis across diverse regions and applications, it is imperative to develop effective methods for their detection and elimination.

Numerous studies have examined the impact of clouds and cloud shadow effects by applying multitemporal reconstruction techniques based on tensor factorization and deep learning methods (Lin et al., 2022; Zhang et al., 2021, 2020). These methods leverage temporal redundancy to reconstruct cloud-free imagery and reduce the influence of atmospheric obstructions. Although such techniques have demonstrated robust performance, they generally require multitemporal datasets and involve considerable computational complexity.

In addition to the aforementioned applications, Sentinel-2 imagery is extensively used in food security research, encompassing studies on agricultural productivity and large-scale grazing livestock systems, which constitute two essential pillars of global agri-food systems.

In crop production, Sentinel-2 imagery is widely used for crop type classification and mapping, parcel-level land-use identification, and yield forecasting through time-series analysis, spectral indices, and advanced machine learning and deep learning algorithms. These applications have established Sentinel-2 as a vital data resource for agricultural surveillance and the development of high-resolution-derived products (Feng et al., 2019; Gumma et al., 2022; Maponya et al., 2020; Perich et al., 2023; Singh et al., 2022).

In the field of livestock management, numerous studies have demonstrated the applicability of Sentinel-2 imagery, combined with machine learning techniques and vegetation index analysis, for the quantitative and qualitative monitoring of forage resources. These studies encompass a broad spectrum of applications, including the estimation of forage biomass, assessment of forage quality through crude protein and fiber content, analysis of grassland productivity, and detection of overgrazing (Dusseux et al., 2022; Harmse et al., 2022; İleri and Koç, 2022; Irisarri et al., 2025).

This study aimed to develop and evaluate a novel spectral index for cloud shadow filtering in landscapes predominantly characterized by agriculture and grasslands. To this end, a novel normalized spectral index, referred to as the Cloud Shadow Detection Index (CLOSDI), is

proposed based on the relationship between NDVI and EVI2 to enhance the identification of pixels affected by cloud shadows in these production-oriented environments.
The application of this index supports the production of more precise and consistent shadow masks, thereby minimizing both false negatives and false positives generated by the SCL algorithm. This enhancement improves the quality of Sentinel-2-derived products, such as vegetation time-series, land cover maps, phenological models, and agricultural productivity assessments.
Furthermore, the simplicity of its implementation on platforms such as the Google Earth Engine permits integration into automated processing pipelines, thereby supporting extensive applications in environmental monitoring, precision agriculture, and climate change research. Moreover, its reliance on a spectral index approach allows for adaptation to analogous sensors, including Landsat 8 and 9 and MODIS, thus extending its applicability beyond the scope of the Copernicus program.
In this regard, the proposed index represents a versatile, reproducible, and computationally efficient instrument for addressing one of the principal challenges in optical remote sensing: interference caused by shadows cast by clouds.

2. Materials and methods

2.1. CloudSEN12

The development of data science and machine learning solutions fundamentally relies on access to high-quality data, which constitutes essential input for model training. However, requisite data are not publicly accessible or do not exist in numerous instances. The objective of this study was to enhance the detection of cloud shadow regions in Sentinel-2 imagery.
For this purpose, the publicly accessible dataset CloudSEN12 (CS12) was used, which comprised Sentinel-2 images annotated with labels for clouds and cloud shadows. CS12 is a comprehensive global dataset specifically designed to improve the semantic segmentation of clouds and shadows within Sentinel-2 imagery, thereby supporting the development and assessment of various algorithms.
Unlike other datasets, CS12 comprises more than 49,000 image patches from diverse geographic regions under varying cloud cover, thereby capturing a wide range of atmospheric conditions and surface types (Aybar et al., 2022). The CS12 patches combine Sentinel-2 data (levels 1C and 2A), Sentinel-1 data, digital elevation models, land cover maps, and water bodies, providing a robust contextual basis for classification tasks. The patches span the 2018–2020 period.
Each patch has a size of 5,090 × 5,090 m. The annotations were produced by a team of 14 experts using interactive tools and active learning methods, thereby yielding high-quality pixel-level labels and, in certain instances, partial annotations such as scribbles.
The semantic categories in CS12 are Clear, Thick Cloud, Thin Cloud, and Cloud Shadow (Table 1).

Table 1 Semantic categories defined in the CloudSEN12 dataset.

Code	Category	Description
0	Clear	Pixels without cloud and cloud shadow contamination.
1	Thick Cloud	Opaque clouds block all reflectance from the Earth's surface.
2	Thin Cloud	Semitransparent cloud that alters the surface spectral signal but still allows recognition of the background.
3	Cloud Shadow	Dark pixels are caused by thick or thin clouds.

The dataset is available for free download through the Python package cloudsen12 (pypi.org/project/cloudsen12) or via its official website (cloudsen12.github.io), which also offers sample scripts and pre-trained PyTorch models. The images are arranged in an optimized GeoTIFF (COG) format and include STAC metadata, thereby supporting integration into automated satellite image processing workflows.

The CS12 patch and Sentinel-2 Level-2A (S2-L2A) imagery were processed using Python on the Google Colab platform (colab.google). This complimentary, cloud-based environment enables users to write and execute Python code directly within a web browser, obviating the need for software installation. It is particularly advantageous for data analysis, machine learning, and deep learning applications, providing access to GPU and TPU resources.
Interactive notebooks, such as Jupyter notebooks, support the integration of code, visualizations, and Markdown documentation. Their compatibility with Google Drive further allows for real-time editing and collaboration. In the field of remote sensing, the Google Earth Engine is often used in conjunction with remote sensing tools to acquire, analyze, and process satellite imagery.
Access to the CS12 patches and their associated Sentinel-2 imagery was obtained using the Google Earth Engine (earthengine.google.com) via Google Colab. This platform offers planetary-scale geospatial analysis capabilities and supports the processing and visualization of extensive satellite data without the need for local infrastructure.
Google Earth Engine offers access to a comprehensive collection of imagery and environmental variables, accompanied by sophisticated analytical tools through JavaScript and Python interfaces. It is extensively used in research related to climate change, deforestation, agriculture, water management, and environmental monitoring (Gorelick et al., 2017).
The satellite figures presented in this study were generated using QGIS 3.28.11-Firenze.
The CS12 dataset is structured into three levels of annotation.

(i) High quality: 10,000 patches with comprehensive pixel-level annotations.
(ii) Scribble: 10,000 patches are annotated with quick strokes or sketch-like labels.
(iii) Unlabeled: 29,400 patches lacking manual annotations.

Each image patch depicts a geographic region with varying degrees of cloud cover. For each region of interest, five patches are included, corresponding to different atmospheric conditions: cloud-free (0%), nearly clear (0–25%), low-cloud (25–45%), mid-cloud (45–65%), and fully cloudy (>65%). This stratification ensures the representation of both temporal and spatial variability, which is crucial for training and validating cloud and shadow detection algorithms.
Fig. 1 shows an example patch and its corresponding semantic categories.

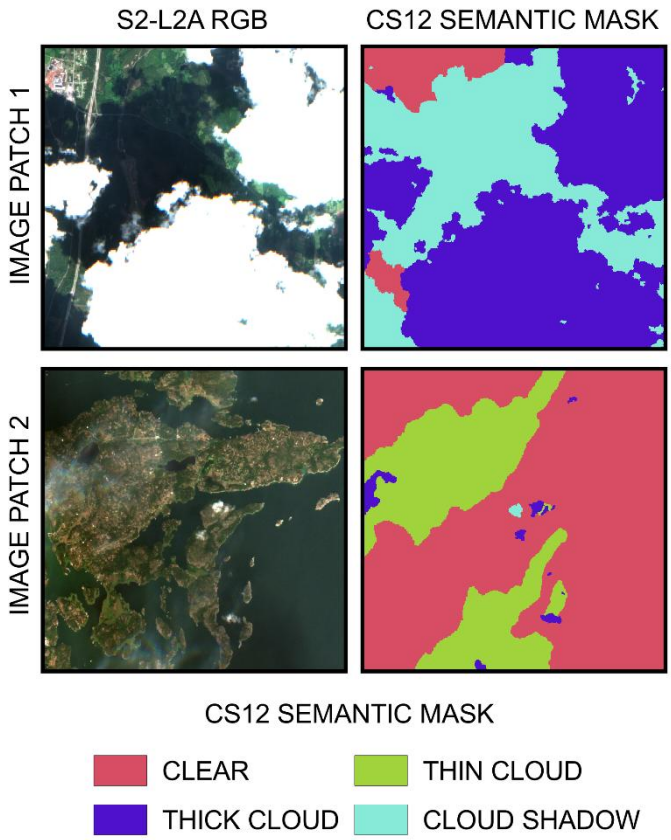

Fig. 1. Examples of CloudSEN12 patches with RGB images and semantic segmentation masks.

Only high-quality patches with complete pixel-level annotations were selected for this study. Of these, patches located in areas with agricultural land use and grassland cover were selected.
To identify these areas, an Ecoregions map (Dinerstein et al., 2017) was used as a reference. This classification system divided the world into 14 biomes. Among these, *temperate grasslands, savannas, and shrublands* and *tropical and subtropical grasslands, savannas, and shrublands* were selected (Fig. 2).
In these biomes, the majority of agricultural crop production and livestock grazing occurs, as illustrated in Figs. 3 and 4.
Of the selected patches, only those with at least 5% of their area obscured by cloud shadows were included. Consequently, 1,231 out of the 10,000 high-quality patches were designated for training and testing.

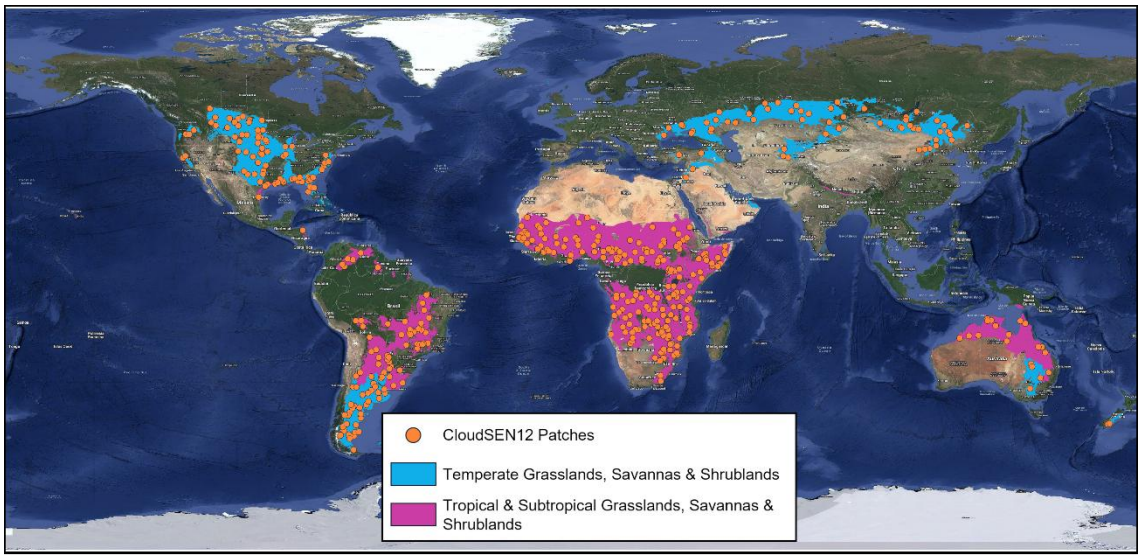

Fig. 2. High-quality CloudSEN12 patches selected for training and testing.

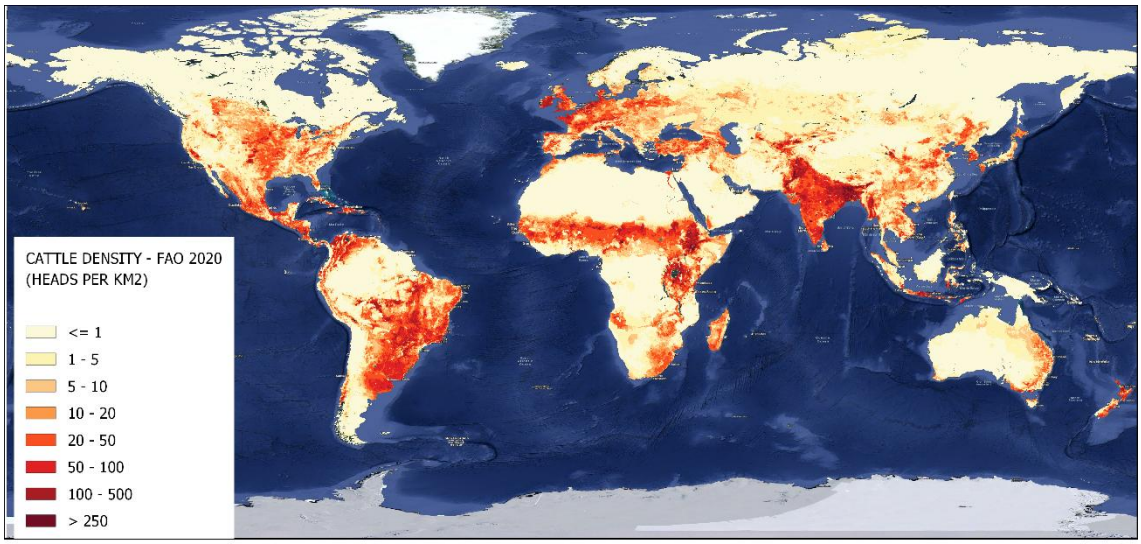

Fig. 3. Global cattle density (Maponya et al., 2020).

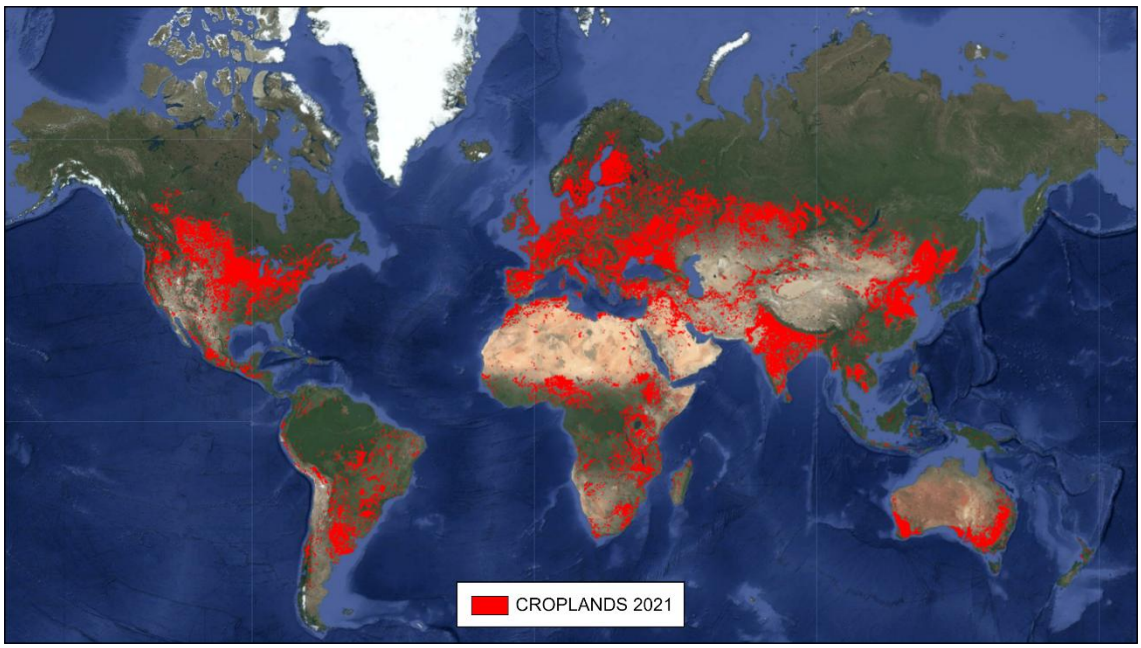

Fig. 4. Global croplands (ESA WorldCereal Consortium, 2021).

The method devised in this study requires the use of binary images known as Binary Shadow Masks (BSM), in which pixels are categorized into two classes: cloud shadow (1) and non-shadow (0). Because the semantic images from CS12 encompass four potential values (see Table 1), they were transformed into binary images (CS12-BSM). For this purpose, pixels with values 0, 1, and 2 (representing Clear, Thick Cloud, and Thin Cloud, respectively) were reclassified as 0, while pixels with value 3 (representing Cloud Shadow) were reclassified as 1, as illustrated in Fig. 5.

2.2. Generation of binary shadow masks from Sentinel-2 Level-2A imagery.

Because the primary aim of this study was to develop a method that enhances the detection of cloud shadows in relation to S2-L2A identification, it was essential to evaluate the performance of the Scene Classification Layer (SCL) in shadow detection using the BSMs generated from CS12 as the reference.

In addition to the standard spectral bands (e.g., red, green, and NIR), S2-L2A images incorporate the SCL band, which is produced by the Sen2Cor algorithm (Main-Knorn et al., 2017) during atmospheric correction. This algorithm assigns each pixel to one of 11 classes, including vegetation, non-vegetated areas, water bodies, snow, cloud shadows, and various cloud types (Fig. 5).

The classification relies on thresholds applied to the top-of-atmosphere (TOA) reflectance values of Sentinel-2 spectral bands, as well as on derived indices, such as the NDVI and NDSI. The primary purpose of the SCL band is not to map land cover directly, but to differentiate usable pixels from those affected by atmospheric conditions, thereby supporting more precise correction and scientific analysis of the data.

Similar to the semantic masks from CS12, it was essential to transform the SCL band into a Binary Shadow Mask (SCL-BSM). In this transformation, pixels corresponding to the classes ' dark area pixels' (2) and ' cloud shadows' (3) were assigned a value of 1, indicating cloud shadow, whereas all other classes were designated as 0, signifying non-shadow.

For each selected CS12 patch, the corresponding SCL patch from S2-L2A was extracted and converted into an SCL-BSM. This approach yielded comparable shadow mask pairs, one derived from CS12 (CS12-BSM) and the other from the SCL band (SCL-BSM).

Fig. 5 shows a representative CS12 patch, along with its RGB image, CS12 semantic mask, CS12-BSM, SCL band, and the resulting SCL-BSM following the conversion.

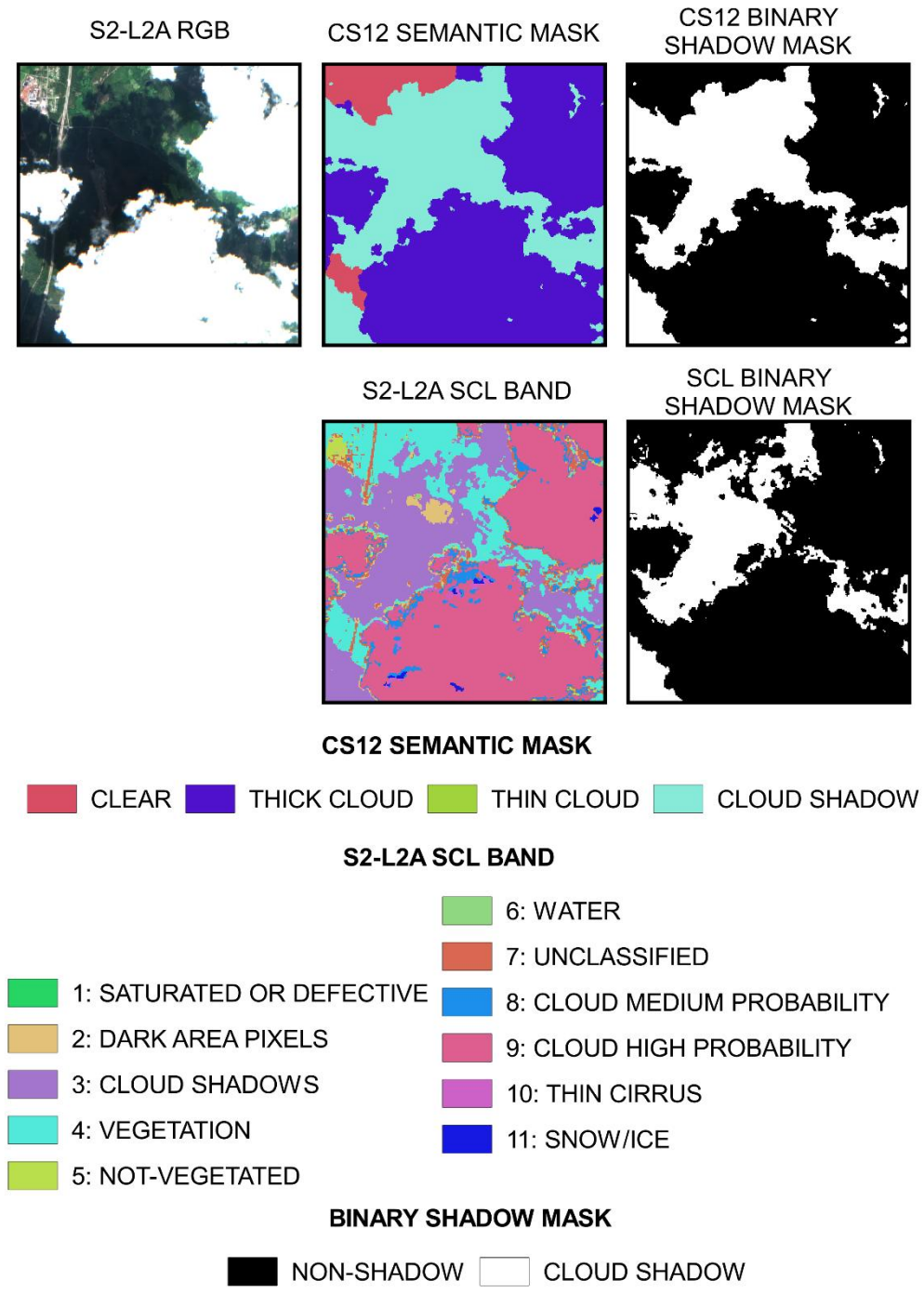

Fig. 5. Conversion of the Sentinel-2 L2A SCL band and CS12 semantic mask into binary shadow masks (CS12-BSM and SCL-BSM).

2.3. Formulation of the Cloud Shadow Detection Index (CLOSDI)

The motivation for this study originated from the observation that the SCL band exhibits limitations in precisely identifying all regions affected by cloud shadows. Fig. 5 illustrates an example in which the SCL-BSM does not fully detect shadow-affected areas, whereas the corresponding CS12-BSM succeeds.

The analysis of images depicting the spectral indices revealed that the Enhanced Vegetation Index (EVI) and Normalized Difference Vegetation Index (NDVI), derived from Sentinel-2 data,

indicated markedly reduced EVI values in vegetated regions affected by cloud shadows. In contrast, NDVI values were less affected in these regions than in vegetated areas free of shadows. This difference indicates distinct behavior between the two indices when shadows are present, supporting the conceptual basis of this study: using this difference to develop a new index that more precisely identifies cloud-shadowed areas and exceeds the detection capabilities of the SCL band.

Both EVI and NDVI (Eq. (1) and (2)) are derived from the combinations of surface reflectance within the BLUE, RED, and NIR spectral bands. EVI further includes atmospheric correction coefficients aimed at minimizing the effects of aerosol scattering and background interference (Didan et al., 2015).

$$EVI = 2.5\frac{NIR-RED}{NIR+6RED-7.5BLUE+1} \quad (1)$$

$$NDVI = \frac{NIR-RED}{NIR+RED} \quad (2)$$

Regarding EVI, the BLUE band presents difficulties because of its heightened sensitivity to aerosols and other atmospheric pollutants, which complicates the process of atmospheric correction. To address these challenges, some researchers have proposed a simplified variant, EVI2 (Eq. (3)), which excludes the BLUE band while preserving the soil-adjustment and linearization features of the original index (Jiang et al., 2008).

$$EVI2 = 2.5\frac{NIR-RED}{NIR+2.4RED+1} \quad (3)$$

Because EVI2 does not necessitate the BLUE band and is more straightforward to implement, it was selected for this study.

Sentinel-2 spectral data are presented as digital numbers encoded in a 16-bit integer format. These values denote scaled reflectance and must be converted to physical surface reflectance by dividing by a scale factor of 10,000, resulting in unitless reflectance values that typically range between 0 and 1 (European Space Agency (ESA), 2021a; Google Earth Engine, 2024). As spectral indices are defined based on reflectance, all index calculations in this study were conducted using reflectance values rather than digital numbers.

Prior to the development of the new index, a comprehensive search was conducted to determine whether any existing index integrated EVI/EVI2 and NDVI. Several sources were consulted, including

- The standardized Awesome Spectral Indices (ASI) catalog, accessible at https://awesome-ee-spectral-indices.readthedocs.io/en/latest/index.html, comprises over 230 indices used in Earth system research (Awesome Spectral Indices, n.d.).
- The Sentinel Hub index database can be accessed at: https://custom-scripts.sentinel-hub.com/custom-scripts/sentinel-2/indexdb.
- Google Scholar search engine.
- The Deep Research tool developed by OpenAI can be accessed at: https://openai.com/index/introducing-deep-research.

None of these resources included an index that contained the following equation:

$$\frac{NDVI-EVI}{NDVI+EVI} \text{ or } \frac{NDVI-EVI2}{NDVI+EVI2}$$

Therefore, a novel index, termed the Cloud Shadow Detection Index (CLOSDI), is proposed, as defined by the following equation:

$$CLOSDI = \frac{NDVI-EVI2}{NDVI+EVI2}100 \quad (4)$$

CLOSDI can be characterized as a composite normalized index, given that it uses a normalized difference between two vegetation indices (NDVI and EVI2) rather than directly applying to RED and NIR reflectance values. By substituting the definitions of NDVI and EVI2 into Eq. (4), extracting and canceling the common term (NIR−RED), and simplifying through the clearance of denominators, CLOSDI can be expressed as a closed-form function that is a function of only RED and NIR reflectance, as demonstrated below.

$$CLOSDI = \frac{1-1.5NIR-0.1RED}{1+3.5NIR+4.9RED}100 \quad (5)$$

This reformulation (Eq. (5)) is algebraically equivalent to Eq. (4) and permits CLOSDI to be determined directly from RED and NIR reflectance readings without the need to explicitly calculate the NDVI and EVI2 indices.

Under specific conditions, particularly with clouds, both the RED and NIR reflectance values can become significantly high and similar in magnitude, resulting in NDVI and EVI2 values that are close to zero. In such scenarios, Eq. (4), which is formulated based on these indices, may encounter division-by-zero issues or numerical instability when the denominator approaches zero. Conversely, Eq. (5), which is directly expressed as a function of RED and NIR reflectance, does not have this limitation, as its denominator remains strictly positive for all reflectance values.

Fig. 6 presents examples of RGB, NDVI, EVI2, and CLOSDI for a representative patch, including the point locations used for spectral analysis. Table 2 and Fig. 7 demonstrate a clear and consistent pattern in the behavior of spectral bands and indices across clear sky, thick cloud cover, and cloud shadow conditions. In regions affected by cloud shadows, reflectance values in both the RED and NIR bands are significantly diminished compared with clear vegetation, with a notably greater reduction observed in the NIR band (-19.5 units) than in the RED band (-2.4 units).

Although both NDVI and EVI2 are derived from RED and NIR reflectance, their responses to shadow conditions differ substantially because of their mathematical formulations. NDVI exhibits a moderate decrease (-18.8 units) owing to its normalized difference structure, which partially compensates for simultaneous reductions in both spectral bands. In contrast, EVI2 shows a much larger decrease (-30.3 units), reflecting its formulation as a weighted reflectance ratio with an additive constant, which increases its sensitivity to absolute reductions in reflectance, particularly in the NIR band.

Owing to the varying sensitivity levels, the disparity between NDVI and EVI2 is markedly accentuated in the presence of cloud shadows. This results in considerably elevated CLOSDI values within shadowed regions, averaging 73.1, in contrast to the values observed in clear vegetation, which average 30.8. Such an increase of 42.3 units underscores the pronounced distinction between shadowed and non-shadowed vegetation. Conversely, areas affected by thick clouds demonstrate negative CLOSDI readings (-5.0), thereby distinguishing them from both vegetation and cloud-shadowed regions. This consistent and physically plausible behavior, observed in both individual point measurements and average spectral signatures, substantiates the robust capability of CLOSDI to discriminate vegetation influenced by cloud shadows from other surface conditions.

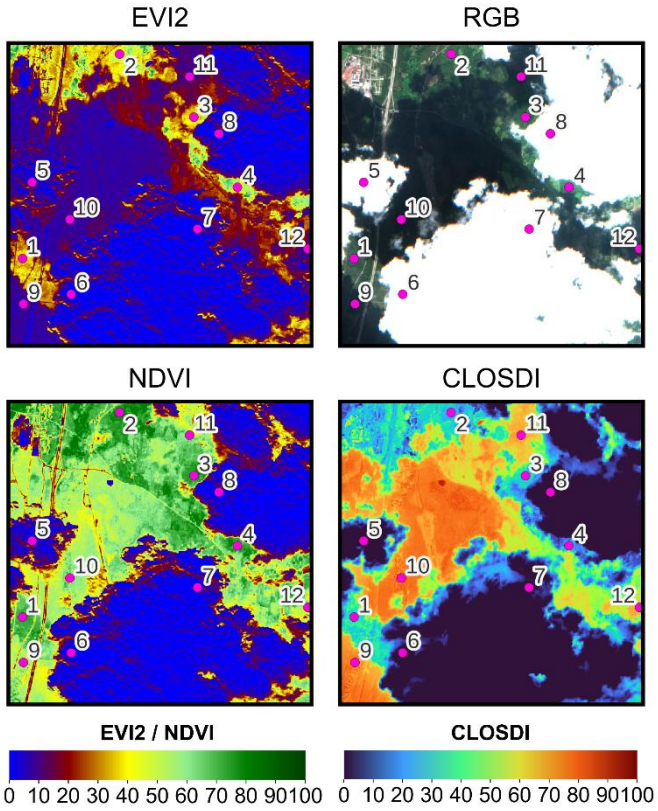

Fig. 6. CloudSEN12 patch with corresponding RGB, EVI2, NDVI, and CLOSDI images.

Table 2 presents the spectral values, vegetation indices, and CLOSDI for clear, thick cloud, and cloud shadow points within a representative patch.

Point	Category	RED	NIR	NDVI	EVI2	CLOSDI
1	Clear	3.6	22.2	72.3	35.6	34.1
2		5.0	30.5	72.0	44.8	23.3
3		3.0	21.0	75.2	35.1	36.3
4		4.2	25.3	71.7	39.0	29.5
	Average	4.0	24.8	72.8	38.6	30.8
5	Thick cloud	85.7	91.6	3.3	3.7	-5.5
6		95.9	94.1	-1.0	-1.1	-5.6
7		78.7	86.7	4.9	5.4	-4.8
8		87.1	82.3	-2.8	-3.1	-3.9
	Average	86.9	88.7	1.1	1.2	-5.0
9	Cloud shadow	1.5	4.6	50.8	7.2	75.2
10		1	3.8	58	6.6	79.5
11		1.7	6.4	58.8	10.7	69.2
12		2.1	6.2	48.6	9	68.6
	Average	1.6	5.3	54.1	8.4	73.1
Difference Cloud shadow-Clear		-2.4	-19.5	-18.8	-30.3	42.3
Difference Cloud Shadow-Thic cloud		-85.3	-83.4	53.0	7.2	78.1

Note: RED, NIR, NDVI, and EVI2 are expressed as values multiplied by 100. Differences were calculated as the average values.

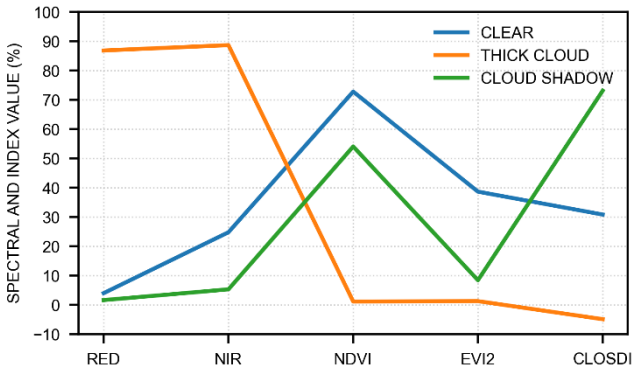

Fig. 7. Average spectral signatures for clear, thick cloud, and cloud shadow points within a representative patch.

2.4. Identifying the best segmentation threshold for CLOSDI

Once the CS12-BSM, SCL-BSM, EVI2, NDVI, and CLOSDI were obtained for each patch in the training set, the optimal cutoff threshold (OCT) was determined. This threshold defines the value above which a pixel is classified as a cloud shadow: if a pixel's CLOSDI value is equal to or exceeds the OCT, it is classified as a cloud shadow (1); otherwise, it is classified as a non-shadow (0).

Fig. 8 illustrates this procedure and demonstrates how various thresholds (20, 30, 50, and 70) influence the same patch. As shown, a low threshold (e.g., 20) tends to overestimate shadow extent and erroneously classifies numerous regions as shadows. Conversely, a high threshold (e.g., 70) tends to underestimate shadow extent and thereby omits many actual shadowed areas.

In this instance, the OCT appeared to fall within the 30–50 range. However, such visual adjustment is applicable only in specific cases. For large datasets comprising thousands of images, as in this study, an automated and quantitative method is indispensable.

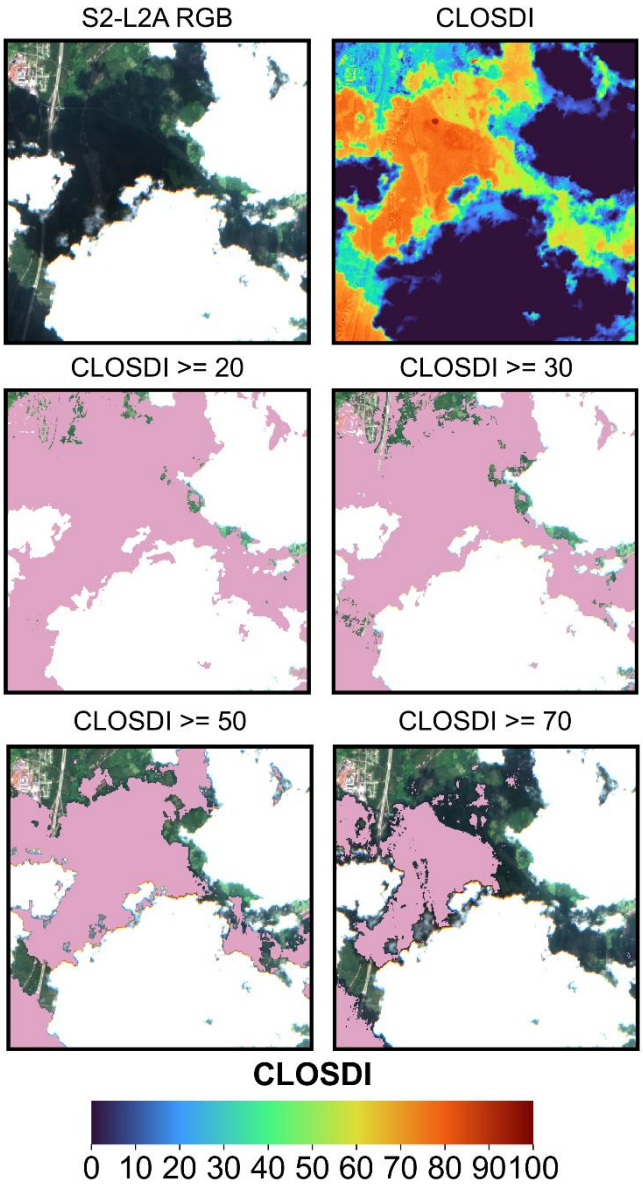

Fig. 8. Visual evaluation of the effect of varying cutoff thresholds on a patch.

Accordingly, the 1,231 selected patches were divided into two subsets using an 80/20 split.

- A total of 984 patches (80%) were used for training and the determination of the OCT.
- The remaining 247 patches (20%) were designated for testing and were not included in the threshold calibration.

During the training phase, threshold values ranging from 1 to 99 were evaluated, with a single run conducted for each value. In each execution, a BSM was generated for each patch using the CLOSDI index and the corresponding threshold.
The validity of each binary mask was quantified using the Jaccard index (da Fontoura Costa, 2021), also known as the intersection over union (IoU) (WEI and HU, 2024). This metric assesses the similarity between two sets, A and B, and is formally defined as follows:

$$IoU = \frac{|A \cap B|}{|A \cup B|} \tag{6}$$

In segmentation tasks, the IoU quantifies the overlap between an automated segmentation and a reference segmentation. In this study, the automated segmentation pertains to the mask generated by CLOSDI, whereas the reference segmentation corresponds to CS12-BSM. It is extensively used because of its simplicity, computational efficiency, and straightforward interpretability: a value of 0 signifies no overlap, whereas 1 denotes perfect correspondence. This metric has been used in recent studies on satellite image segmentation (Mazza et al., 2021; Montero et al., 2023; Nambiar et al., 2022).
Figure 9 shows an example of the intersection over union (IoU) computation for a training image patch.

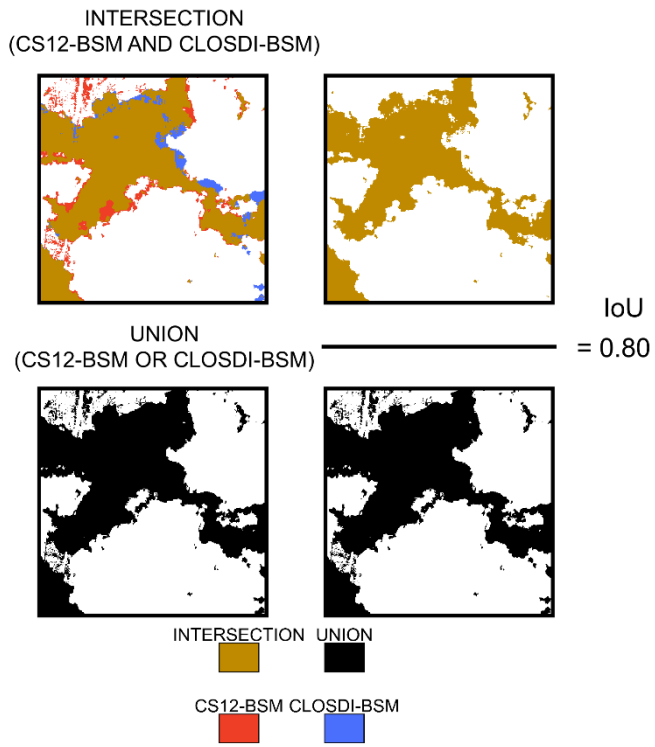

Fig. 9. Illustration of the intersection over union (IoU) calculation between a CLOSDI-BSM mask and its CS12-BSM reference mask.

In each iteration, 984 IoU values, corresponding to individual patches, were computed and expressed as percentages to augment interpretability. The median of these values was adopted as the performance metric at the respective threshold. This method yielded an IoU threshold performance curve.
Fig. 10 illustrates the comprehensive workflow of the training procedure and OCT search. The threshold that maximized the IoU was chosen as the OCT for generating masks for the test set.
Finally, to assess the capability of the CLOSDI index in detecting cloud shadows, five commonly used performance metrics were used: precision, recall, F1-score, IoU, and balanced overall accuracy (BOA). The initial three metrics were calculated in accordance with previously established criteria (Sokolova and Lapalme, 2009), whereas BOA was adopted as specified in the CS12 benchmark (Aybar et al., 2022).
These metrics were computed for CLOSDI-BSM and SCL-BSM. Consequently, using the CS12-BSM (derived from expert-labeled data) as a benchmark, the performances of both methods were systematically compared.
The complete workflow for the testing phase is shown in Fig. 11.

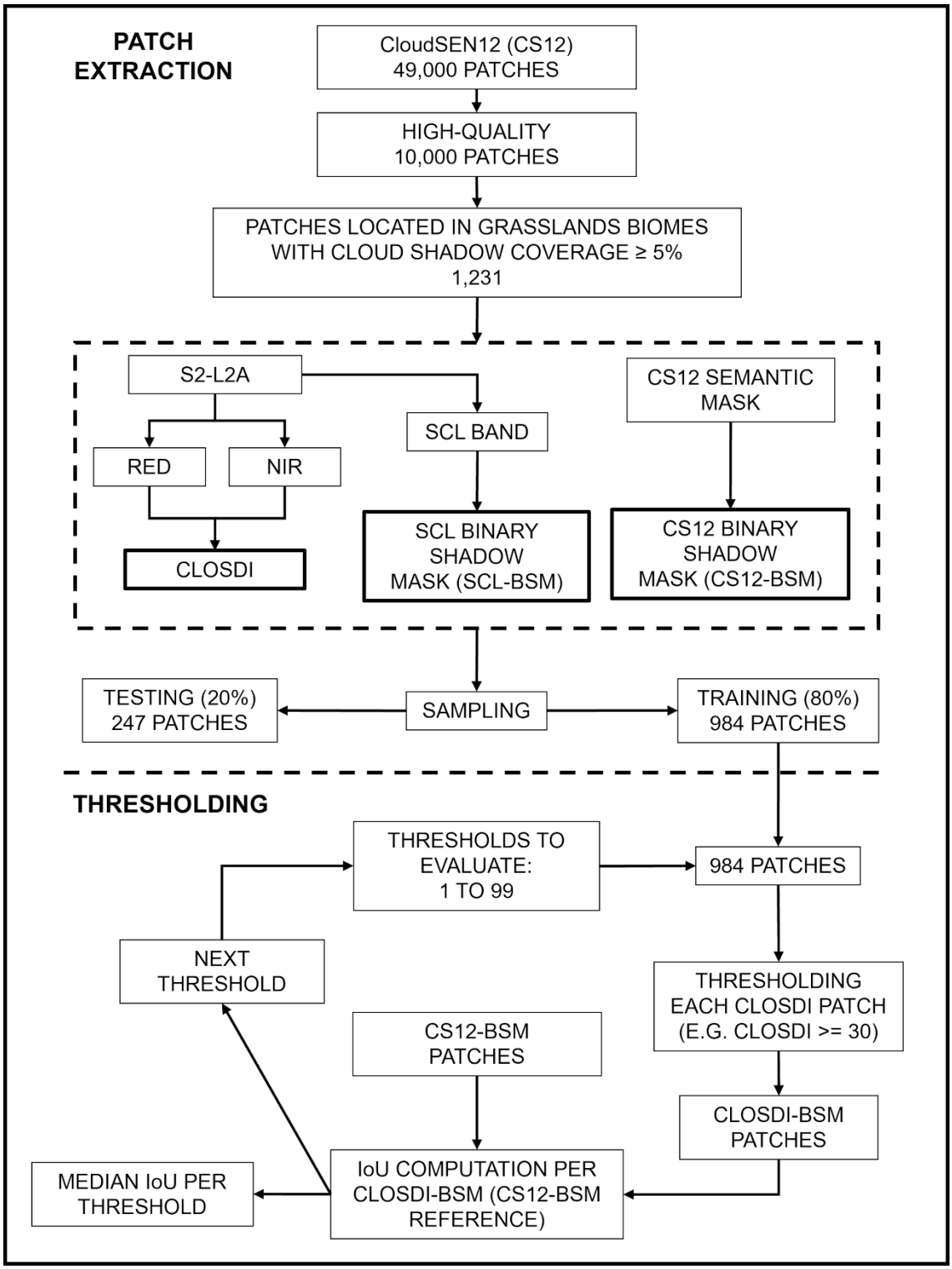

Fig. 10. Workflow of the training process and selection of the optimal cutoff threshold.

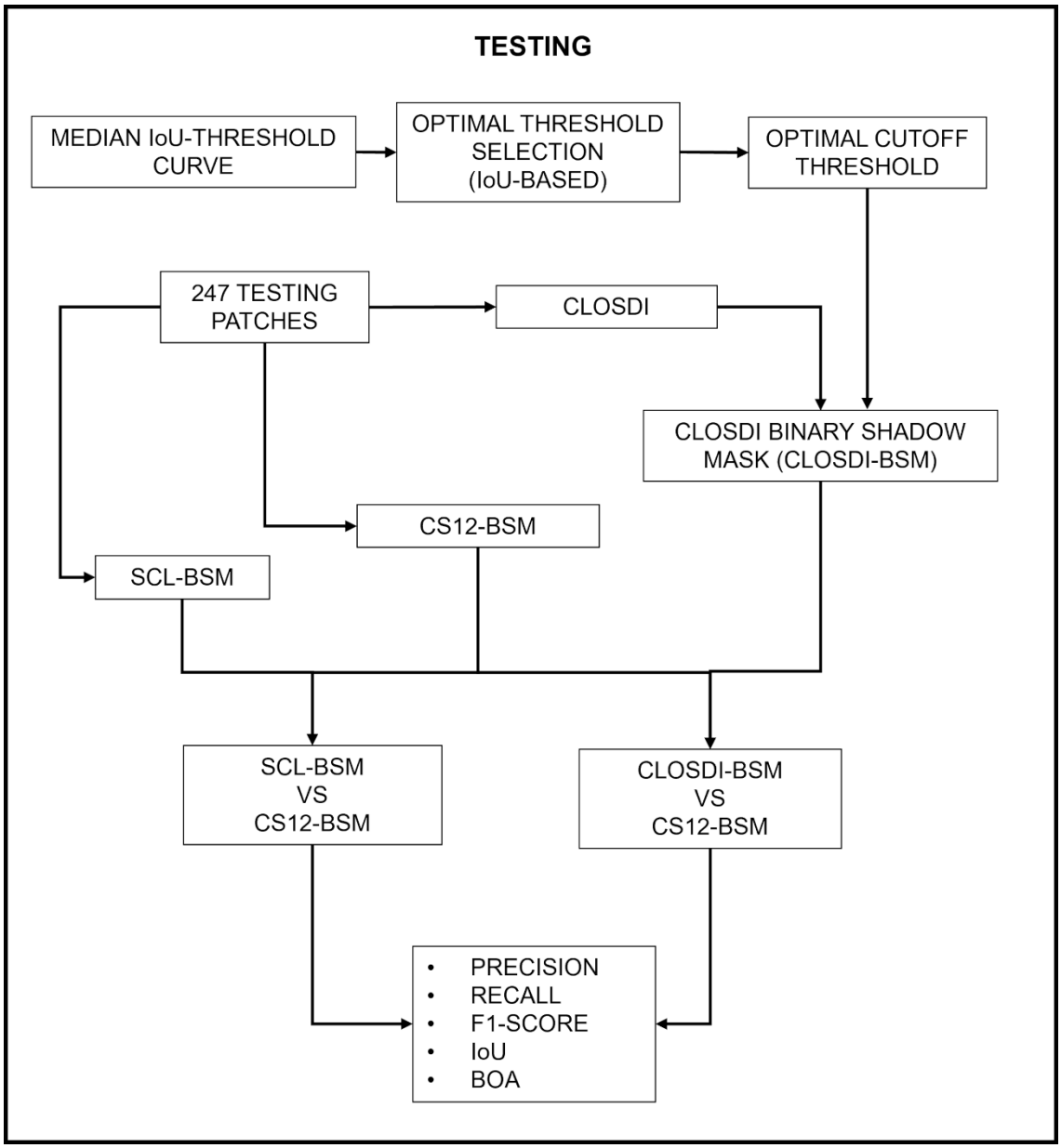

Fig. 11. Workflow of CLOSDI and SCL performance evaluation on the test set.

3. Results and discussion

After training to identify the OCT, a plot illustrating the median IoU in relation to the CLOSDI cutoff threshold was generated, as shown in Fig. 12. This plot shows the median IoU for each iteration as a function of the CLOSDI cutoff threshold. Additionally, a fitted curve based on the observed median IoUs was incorporated. From this curve, the optimal OCT, which maximizes the IoU, was determined to be 34.0, with an IoU value of 50.1. As shown in the plot, the IoU exhibits a sharp increase from a threshold of 10, reaches its peak at 34.0, and subsequently declines rapidly to zero as the threshold exceeds 65.

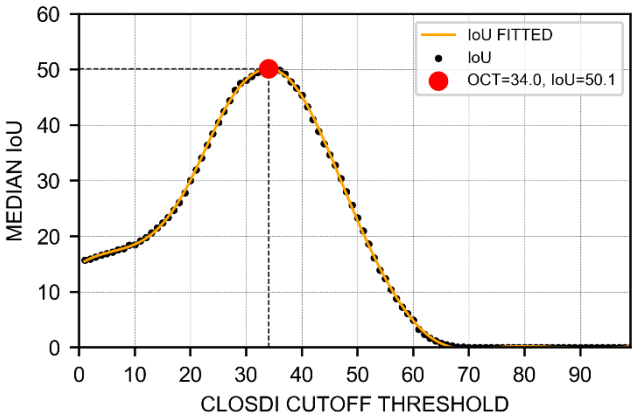

Fig. 12. Performance curve (median IoU) as a function of CLOSDI cutoff threshold during training.

The CLOSDI values ranged from -15.6 to 99.0 across the training set, reflecting a broad dynamic range under varying illumination conditions. This range provides additional context for interpreting the selected threshold and confirms that CLOSDI captures substantial variability in the spectral response across the analyzed patches.

Once the OCT value was determined, the subsequent step involved assessing it on the test set in accordance with the procedures outlined in the workflow shown in Fig. 11. This evaluation was conducted using the reference CS12-BSM, the corresponding SCL-BSM, and the newly generated masks obtained by applying the CLOSDI ≥ 34.0 threshold (CLOSDI-BSM). Both the SCL-BSM and CLOSDI-BSM were compared with the reference CS12-BSM, and the following performance metrics were computed for each test patch: precision (Eq. (7)), recall (Eq. (8)), F1-score (Eq. (9)), IoU, and BOA (Eq. (10)).

$$Precision = \frac{TP}{TP+FP} \tag{7}$$

$$Recall = \frac{TP}{TP+FN} \tag{8}$$

$$F1 - Score = 2 \cdot \frac{P \cdot R}{P+R} \tag{9}$$

$$BOA = 0.5 \cdot (P + R) \tag{10}$$

TP, *FP*, *FN*, *P*, and *R* denote true positive, false positive, false negative, precision, and recall, respectively.

Because the performance metrics were computed for each individual test patch, Fig. 13 presents the median values of these metrics. As illustrated, CLOSDI surpassed SCL in all metrics, except for precision. SCL achieved a precision score of 91.5%, surpassing CLOSDI's score of 69.9 by 21.6 percentage points. This discrepancy suggests that SCL is more effective than CLOSDI in correctly identifying pixels that are true cloud shadows among those classified as such.

In the case of recall, the situation is reversed, with a notable discrepancy between CLOSDI (76.8) and SCL (19.6). Performance on true cloud shadow pixels is significantly deficient for SCL, resulting in a high omission rate.

CLOSDI, in comparison with SCL, demonstrates a more balanced performance between precision and recall, although it exhibits a marginally superior recall, rendering it more susceptible to commission errors relative to omission errors, which results in a higher number of pixels being classified as cloud shadows when they are not. Its F1-score is 62.1. Conversely, SCL recorded a considerably lower F1-score of 19.6, primarily because of a markedly low recall and a high rate of omission errors.

Similarly, the IoU (45.0 vs. 16.7) and BOA (80.1 vs. 57.6) metrics further substantiate CLOSDI's superior overall performance compared to that of SCL.

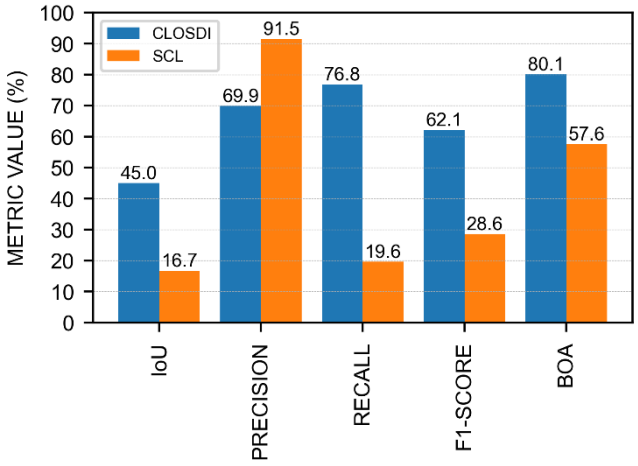

Fig. 13. Comparison of the median performance metric values of CLOSDI and SCL on the test set.

As Fig. 13 displays the median values of the performance metrics, Table 3 and Fig. 14 offer a more comprehensive characterization of the IoU distribution through descriptive statistics and violin plots. An initial observation from the violin plots is that the IoU distributions for both CLOSDI and SCL are non-normal. For CLOSDI, values below the median exhibited greater variability than those above it, indicating an asymmetric distribution with a longer lower tail. Conversely, the SCL distribution demonstrated greater variability to the right of the median, whereas values below the median were heavily compressed, resulting in a noticeable accumulation of low-IoU cases.

Regarding the descriptive statistics, the minimum and maximum IoU values were comparable between the two methods. However, CLOSDI achieved a marginally higher maximum than SCL (87.4 vs. 83.8). More pronounced differences were evident in the interquartile range. CLOSDI consistently surpassed SCL across all measures of central tendency and variability, with notably higher values for Q1 (25.2 vs. 0.1), median (46.4 vs. 16.7), and Q3 (65.1 vs. 48.2). The near-zero Q1 value observed in SCL indicates that a significant proportion of test patches displayed severe performance degradation, aligning with the known limitations of the SCL algorithm in detecting cloud shadows.

Although both methods exhibit comparable extreme values, the disparities in the internal structure of their distributions suggest that the CLOSDI's enhanced performance is systematic rather than attributable to isolated instances. In addition to achieving higher median IoU values, the CLOSDI demonstrated a more favorable and stable distribution of performance, with a significant proportion of test samples reaching moderate-to-high IoU scores.

Table 3 IoU descriptive statistics for CLOSDI and SCL on the test set.

Method	Minimum	Q1	Median	Q3	Maximum
CLOSDI	0	25.2	46.4	65.1	87.4
SCL	0	0.1	16.7	48.2	83.8

Note: Q1 and Q3 denote the first and third quartiles (25th and 75th percentiles).

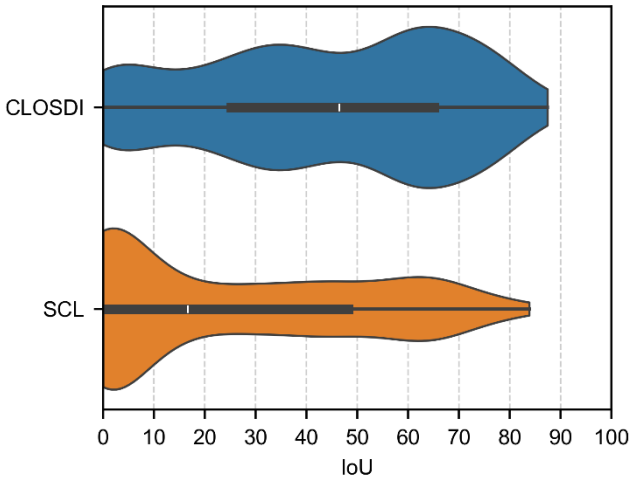

Fig. 14. IoU violin plots for CLOSDI and SCL on test set.

Given that the IoU values obtained with CLOSDI and SCL are paired and their distributions are non-normal, the non-parametric Wilcoxon signed-rank test (King and Eckersley, 2019) was used to evaluate whether a statistically significant difference exists between the two cloud-shadow filtering methods. The null hypothesis states that the median of the paired differences in the IoU values between CLOSDI and SCL is zero. The test results indicated a statistically significant difference between the two methods ($W = 4479$, $p = 1.402 \times 10^{-19}$), thereby rejecting the null hypothesis. In conclusion, these findings demonstrate that CLOSDI offers statistically and practically superior IoU performance compared to SCL across the evaluated test set.

Fig. 15 illustrates the patches randomly selected from the first quartile (Q1), median, third quartile (Q3), and 90th percentile (P90) of the CLOSDI distribution. In these instances, the CLOSDI method consistently outperformed SCL, with the exception of the patch corresponding to Q1.

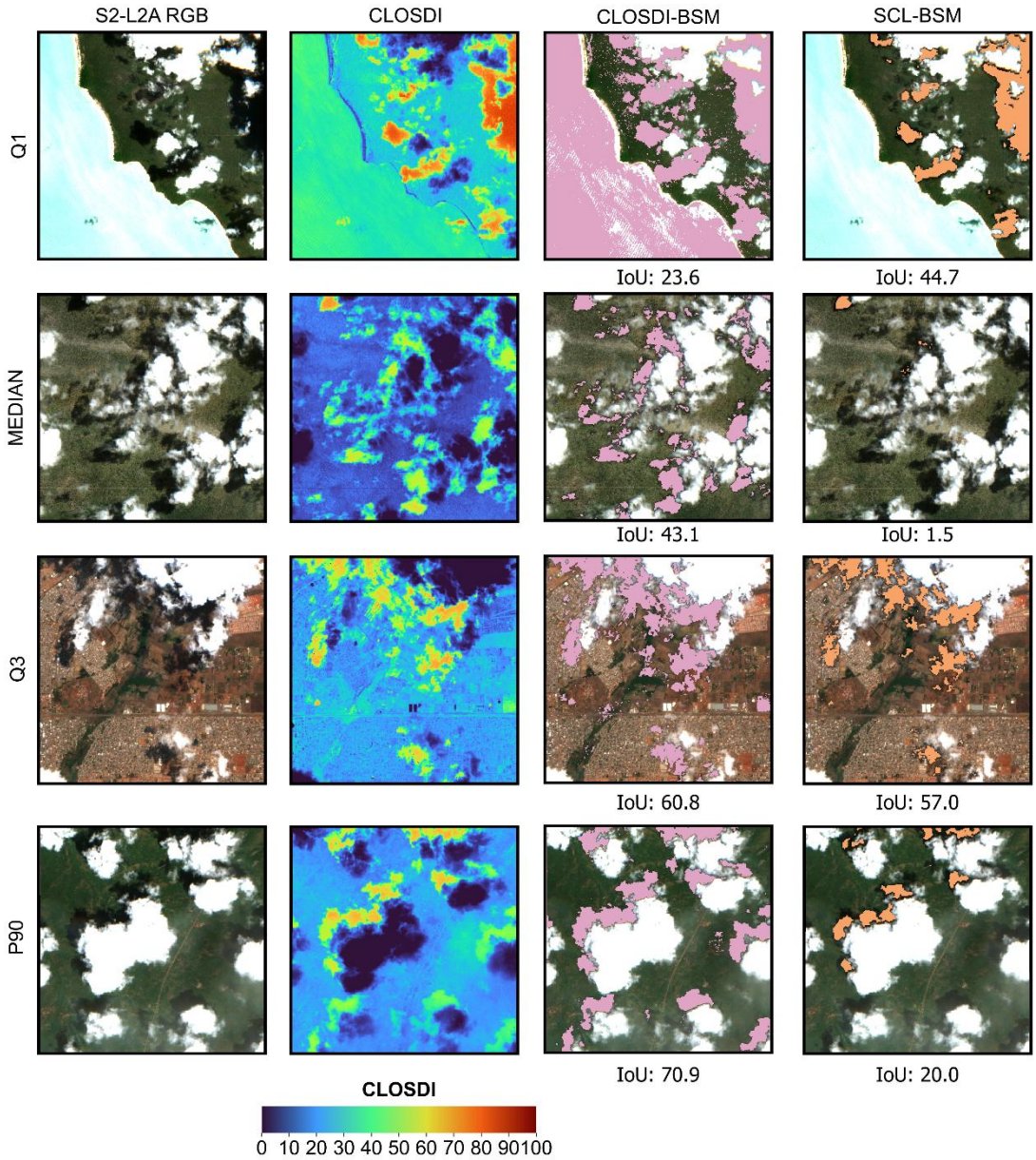

Fig. 15. Comparative analysis of CLOSDI and SCL methods with respect to patches in the test set.

The Wilcoxon test demonstrated that the application of CLOSDI for cloud shadow filtering resulted in markedly superior performance compared to that of SCL. It is pertinent to observe that CLOSDI and SCL are derived from distinct spectral information and depend on fundamentally different approaches.

As explained in the Materials and methods section, CLOSDI was conceptually defined based on the relationship between NDVI and EVI2, which exhibit different sensitivities to shadow conditions in vegetated areas. This formulation offers a clear physical interpretation of the index, as CLOSDI measures the divergence between these two indices under shadow. Nonetheless, CLOSDI can be computed using its algebraically equivalent direct formulation based on RED and NIR reflectance.

In contrast, the SCL band is produced by the Sen2Cor algorithm, which internally consolidates multiple sub-algorithms and adheres to physical principles to categorize pixels into thematic classes, such as water, vegetation, clouds, and cloud shadows. The cloud shadow detection process within Sen2Cor merges radiometric and geometric methods.

Potential cloud shadows are identified radiometrically as dark pixels exhibiting a spectral response in the BLUE, GREEN, RED, NIR, SWIR1, and SWIR2 bands that match or are darker

than a reference shadow spectrum, which is derived from an extensive dataset of cloud shadow examples across various land covers. These candidates are then refined through the application of geometric constraints based on cloud positioning, solar geometry, and cloud height distribution (European Space Agency (ESA), 2021b).

The Sen2Cor cloud shadow detection algorithm uses six spectral bands, whereas CLOSDI requires only two, making Sen2Cor more complex. Nonetheless, the experiments conducted in this study indicated that its performance was inferior. Consequently, CLOSDI delivers superior performance and provides a computationally more straightforward and easily implementable alternative.

Nevertheless, the optimal threshold derived from CLOSDI for cloud shadow filtering generally demonstrates robust performance across most scenarios. However, the violin plot of the test set indicates that the value of 34.0 is not universally optimal in a considerable number of instances. Accordingly, it may be prudent to fine-tune the threshold slightly upward or downward for particular cases based on the specific attributes of the scene.

Finally, Fig. 16 illustrates the median BOA values obtained in this study for the CLOSDI and SCL methods, in comparison with those documented in the CS12 benchmark for a range of algorithms. Although the assessment within CS12 was performed on a different test set than that used herein, the comparison is included to offer a reference point for contextualizing the performance of the CLOSDI method relative to other existing approaches.

As demonstrated, the method developed in this study ranks third overall, being exceeded only by human-level classification (executed by human experts) and the UNetMobV2 approach (Aybar et al., 2022), which is based on deep learning.

The CLOSDI-based method achieves performance levels comparable to those of KappaMask L1C (Domnich et al., 2021) and Fmask (Qiu et al., 2019). Conversely, the SCL exhibited markedly inferior performance, similar to Sen2Cor, the algorithm used to generate the Sentinel-2 SCL band, from which the SCL-BSMs in this study were derived.

Furthermore, the CLOSDI method surpasses KappaMask L2A (Domnich et al., 2021) by a margin of 16 percentage points. It is important to highlight that the proposed approach demonstrates a significantly lower computational complexity than the algorithms assessed in CS12.

By achieving the second-best overall performance when excluding the human level classification, one of CLOSDI's primary advantages becomes apparent: its implementation demands significantly fewer computational resources, does not depend on GPU acceleration as KappaMask and UNetMobV2 do, and is simpler than both Sen2Cor and Fmask.

This trade-off between competitive accuracy and low computational complexity renders the CLOSDI particularly appropriate for large-scale or operational cloud shadow-filtering applications.

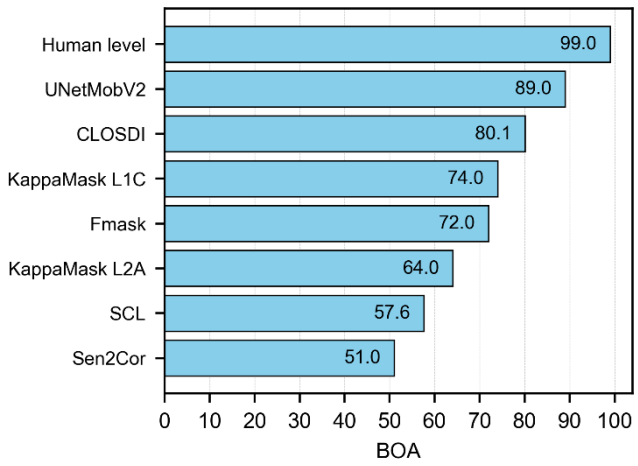

Fig. 16. Comprehensive comparison of BOA among CLOSDI, SCL, and benchmark algorithms from CloudSEN12.

Previous studies have addressed cloud and cloud shadow effects using multitemporal reconstruction techniques based on tensor factorization and deep learning (Lin et al., 2022; Zhang et al., 2021, 2020). These methods aim to reconstruct cloud-free imagery by leveraging temporal redundancy. In contrast, the method proposed in this study emphasizes the direct identification of cloud shadow pixels in single-date imagery using a physically interpretable spectral index. This approach is particularly suitable for operational applications in which multitemporal data may be unavailable or where computational efficiency is essential. In this context, accurate shadow detection using CLOSDI can also support multitemporal reconstruction workflows by providing reliable shadow masks for subsequent image restoration procedures.

Several strengths of the proposed method are worth highlighting. CLOSDI demonstrated markedly superior overall performance relative to the Sentinel-2 SCL band across all evaluated metrics, except for precision, with the improvement confirmed to be systematic by the Wilcoxon signed-rank test. Among the methods assessed in the CS12 benchmark, CLOSDI ranked second when human expert labeling was excluded, achieving a performance comparable to Fmask and KappaMask L1C while surpassing KappaMask L2A by 16 percentage points. This level of performance was achieved with substantially lower computational complexity: the index requires only RED and NIR reflectance, does not depend on GPU resources or large training datasets, and can be readily implemented in automated processing pipelines, including cloud-based platforms such as Google Earth Engine. Furthermore, CLOSDI offers a clear physical interpretation grounded in the differential sensitivity of NDVI and EVI2 to shadow conditions, and its formulation based on fundamental spectral relationships suggests potential adaptability to other optical sensors beyond Sentinel-2.

Notwithstanding these strengths, several limitations of this study must be acknowledged. First, CLOSDI was developed and evaluated exclusively on patches from temperate and tropical grassland biomes; its performance in other land cover types, such as forests, urban areas, bare soils, or water bodies, has not been assessed. Second, as the index is based on the differential sensitivity of NDVI and EVI2 to shadow conditions, its applicability is inherently restricted to vegetated surfaces, and it is not expected to perform reliably under non-vegetated conditions. Third, although the OCT of 34.0 was found to perform well across most cases, it was not universally optimal, as evidenced by the lower-tail variability observed in the IoU distribution of the test set; scene-specific adjustments may therefore be required under certain conditions. Fourth, while CLOSDI demonstrated superior overall performance relative to SCL, a lower precision was observed, indicating a higher rate of commission errors. Finally, although CLOSDI shows potential for adaptation to other optical sensors, such as Landsat and MODIS, this has not yet been validated, and transferability to other platforms cannot be assumed without further evaluation.

4. Conclusions

This study presents and assesses CLOSDI, a novel spectral index developed to enhance the detection of cloud shadows in Sentinel-2 imagery within agricultural and grassland-dominated landscapes. The index was conceptually formulated from the differential sensitivity of NDVI and EVI2 to shadow conditions and reformulated into a closed-form expression based solely on RED and NIR reflectance, ensuring numerical stability and computational efficiency.

The results demonstrated that CLOSDI markedly outperformed the Sentinel-2 SCL band in cloud shadow detection, offering a more balanced and resilient performance across the evaluated metrics. When compared with state-of-the-art methods assessed on the CS12 benchmark, CLOSDI ranked among the top-performing approaches, surpassed only by human expert labeling and deep learning methods, while requiring substantially lower computational resources.

CLOSDI offers several advantages, including simplicity and physical interpretability. Requiring only RED and NIR reflectance, it can be readily applied in automated satellite image processing pipelines, including platforms such as Google Earth Engine. Furthermore, its formulation based on fundamental spectral relationships suggests potential adaptability to other optical sensors, such as Landsat and MODIS.

Future research may examine adaptive threshold selection strategies, assess CLOSDI performance across a wider range of land cover types, and explore their integration with machine learning frameworks to further improve cloud shadow detection performance.

Conflict of Interest

The author declares no conflict of interest.

Funding sources

This research did not receive any specific grant from funding agencies in the public, commercial, or not-for-profit sectors. The work was carried out as part of the author's regular activities at the Instituto Nacional de Investigación Agropecuaria (INIA, Uruguay).

Data availability

All data used in this work come from published and open-access sources and are fully attributed. Sentinel-2 imagery was accessed via the Google Earth Engine platform (https://earthengine.google.com), and the CloudSEN12 benchmark dataset (Aybar et al., 2022) was used for validation and is publicly available at https://cloudsen12.github.io/

Author Contribution

The author performed all aspects of the research, including conceptualization, methodology, data analysis, programming, validation, visualization, and writing of the manuscript.

Acknowledgements

The author gratefully acknowledges the institutional support of the Instituto Nacional de Investigación Agropecuaria (INIA, Uruguay) and the availability of open-access resources such as the Google Earth Engine platform and the CloudSEN12 project (https://cloudsen12.github.io/), which made this research possible. The author also thanks the remote sensing research community for their continuous efforts in promoting open and reproducible science.

References

Awesome Spectral Indices, n.d. Awesome Earth Engine Spectral Indices [WWW Document]. URL https://awesome-ee-spectral-indices.readthedocs.io/en/latest/index.html

Aybar, C., Ysuhuaylas, L., Loja, J., Gonzales, K., Herrera, F., Bautista, L., Yali, R., Flores, A., Diaz, L., Cuenca, N., Espinoza, W., Prudencio, F., Llactayo, V., Montero, D., Sudmanns, M., Tiede, D., Mateo-García, G., Gómez-Chova, L., 2022. CloudSEN12, a global dataset for semantic understanding of cloud and cloud shadow in Sentinel-2. Sci. Data 9, 782. https://doi.org/10.1038/s41597-022-01878-2

Claverie, M., Ju, J., Masek, J.G., Dungan, J.L., Vermote, E.F., Roger, J.-C., Skakun, S. V., Justice, C., 2018. The Harmonized Landsat and Sentinel-2 surface reflectance data set. Remote Sens. Environ. 219, 145–161. https://doi.org/10.1016/j.rse.2018.09.002

Copernicus SentiWiki, n.d. Sentinel-2 Mission [WWW Document]. URL https://sentiwiki.copernicus.eu/web/s2-mission

da Fontoura Costa, L., 2021. Further generalizations of the Jaccard index, arXiv preprint arXiv:2110.09619.

Didan, K., Munoz, A.B., Solano, R., Huete, A., 2015. MODIS vegetation index user's guide (MOD13 series), University of Arizona: Vegetation Index and Phenology Lab.

Dinerstein, E., Olson, D., Joshi, A., Vynne, C., Burgess, N.D., Wikramanayake, E., Hahn, N., Palminteri, S., Hedao, P., Noss, R., Hansen, M., Locke, H., Ellis, E.C., Jones, B., Barber, C.V., Hayes, R., Kormos, C., Martin, V., Crist, E., Sechrest, W., Price, L., Baillie, J.E.M.,

Weeden, D., Suckling, K., Davis, C., Sizer, N., Moore, R., Thau, D., Birch, T., Potapov, P., Turubanova, S., Tyukavina, A., de Souza, N., Pintea, L., Brito, J.C., Llewellyn, O.A., Miller, A.G., Patzelt, A., Ghazanfar, S.A., Timberlake, J., Klöser, H., Shennan-Farpón, Y., Kindt, R., Lillesø, J.-P.B., van Breugel, P., Graudal, L., Voge, M., Al-Shammari, K.F., Saleem, M., 2017. An Ecoregion-Based Approach to Protecting Half the Terrestrial Realm. Bioscience 67, 534–545. https://doi.org/10.1093/biosci/bix014

Domnich, M., Sünter, I., Trofimov, H., Wold, O., Harun, F., Kostiukhin, A., Järveoja, M., Veske, M., Tamm, T., Voormansik, K., Olesk, A., Boccia, V., Longepe, N., Cadau, E.G., 2021. KappaMask: AI-Based Cloudmask Processor for Sentinel-2. Remote Sens. 13, 4100. https://doi.org/10.3390/rs13204100

Dusseux, P., Guyet, T., Pattier, P., Barbier, V., Nicolas, H., 2022. Monitoring of grassland productivity using Sentinel-2 remote sensing data. Int. J. Appl. Earth Obs. Geoinf. 111. https://doi.org/10.1016/j.jag.2022.102843

ESA WorldCereal Consortium, 2021. ESA WorldCereal 10 m v100 (ESA/WorldCereal/2021/MODELS/v100) [WWW Document]. URL https://developers.google.com/earth-engine/datasets/catalog/ESA_WorldCereal_2021_MODELS_v100

European Space Agency, n.d. Sentinel success stories [WWW Document]. URL https://sentinel.esa.int/web/success-stories/list

European Space Agency (ESA), 2021a. Sentinel-2 MSI Level-2A Product Format Specifications.

European Space Agency (ESA), 2021b. Sentinel-2 MSI Level-2A Algorithm Theoretical Basis Document (ATBD).

Feng, S., Zhao, J., Liu, T., Zhang, H., Zhang, Z., Guo, X., 2019. Crop Type Identification and Mapping Using Machine Learning Algorithms and Sentinel-2 Time Series Data. IEEE J. Sel. Top. Appl. Earth Obs. Remote Sens. 12, 3295–3306. https://doi.org/10.1109/JSTARS.2019.2922469

Google Earth Engine, 2024. COPERNICUS/S2_SR_HARMONIZED: Harmonized Sentinel-2 MSI Level-2A Surface Reflectance dataset [WWW Document]. URL https://developers.google.com/earth-engine/datasets/catalog/COPERNICUS_S2_SR_HARMONIZED

Gorelick, N., Hancher, M., Dixon, M., Ilyushchenko, S., Thau, D., Moore, R., 2017. Google Earth Engine: Planetary-scale geospatial analysis for everyone. Remote Sens. Environ. 202, 18–27. https://doi.org/10.1016/j.rse.2017.06.031

Gumma, M.K., Tummala, K., Dixit, S., Collivignarelli, F., Holecz, F., Kolli, R.N., Whitbread, A.M., 2022. Crop type identification and spatial mapping using Sentinel-2 satellite data with focus on field-level information. Geocarto Int. 37, 1833–1849. https://doi.org/10.1080/10106049.2020.1805029

Harmse, C.J., Gerber, H., van Niekerk, A., 2022. Evaluating Several Vegetation Indices Derived from Sentinel-2 Imagery for Quantifying Localized Overgrazing in a Semi-Arid Region of South Africa. Remote Sens. 14, 1720. https://doi.org/10.3390/rs14071720

İleri, O., Koç, A., 2022. Monitoring the available forage using Sentinel 2-derived NDVI data for sustainable rangeland management. J. Arid Environ. 200, 104727. https://doi.org/10.1016/j.jaridenv.2022.104727

Irisarri, J.G.N., Texeira, M.A., Harris, P., Pembleton, K.G., 2025. Satellite-based monitoring of forage quality in grasslands of the United Kingdom using sentinel-2 data and random forest regression. Front. Vet. Sci. 12, 1–9. https://doi.org/10.3389/fvets.2025.1678123

Jiang, Z., Huete, A., Didan, K., Miura, T., 2008. Development of a two-band enhanced vegetation index without a blue band. Remote Sens. Environ. 112, 3833–3845. https://doi.org/10.1016/j.rse.2008.06.006

King, A.P., Eckersley, R.J., 2019. Inferential Statistics III: Nonparametric Hypothesis Testing, in: King, A.P., Eckersley, R.J. (Eds.), Statistics for Biomedical Engineers and Scientists. Elsevier, pp. 119–145. https://doi.org/10.1016/B978-0-08-102939-8.00015-3

Layton, J.C., Wecker, L., Runions, A., Samavati, F.F., 2023. Cloud Shadow Detection via Ray Casting with Probability Analysis Refinement Using Sentinel-2 Satellite Data. Remote Sens. 15, 3955. https://doi.org/10.3390/rs15163955

Li, Z., Shen, H., Weng, Q., Zhang, Y., Dou, P., Zhang, L., 2022. Cloud and cloud shadow detection for optical satellite imagery: Features, algorithms, validation, and prospects. ISPRS J. Photogramm. Remote Sens. 188, 89–108. https://doi.org/10.1016/j.isprsjprs.2022.03.020

Liang, K., Yang, G., Zuo, Y., Chen, J., Sun, W., Meng, X., Chen, B., 2024. A Novel Method for Cloud and Cloud Shadow Detection Based on the Maximum and Minimum Values of Sentinel-2 Time Series Images. Remote Sens. 16, 1392. https://doi.org/10.3390/rs16081392

Lin, J., Huang, T.-Z., Zhao, X.-L., Chen, Y., Zhang, Q., Yuan, Q., 2022. Robust Thick Cloud Removal for Multitemporal Remote Sensing Images Using Coupled Tensor Factorization. IEEE Trans. Geosci. Remote Sens. 60, 1–16. https://doi.org/10.1109/TGRS.2022.3140800

Main-Knorn, M., Pflug, B., Louis, J., Debaecker, V., Müller-Wilm, U., Gascon, F., 2017. Sen2Cor for Sentinel-2, in: Bruzzone, L., Bovolo, F., Benediktsson, J.A. (Eds.), Image and Signal Processing for Remote Sensing XXIII. SPIE, p. 3. https://doi.org/10.1117/12.2278218

Maponya, M.G., van Niekerk, A., Mashimbye, Z.E., 2020. Pre-harvest classification of crop types using a Sentinel-2 time-series and machine learning. Comput. Electron. Agric. 169, 105164. https://doi.org/10.1016/j.compag.2019.105164

Mazza, A., Sepe, P., Poggi, G., Scarpa, G., 2021. Cloud Segmentation of Sentinel-2 Images Using Convolutional Neural Network with Domain Adaptation, in: 2021 IEEE International Geoscience and Remote Sensing Symposium IGARSS. IEEE, pp. 7236–7239. https://doi.org/10.1109/IGARSS47720.2021.9554367

Montero, D., Aybar, C., Mahecha, M.D., Martinuzzi, F., Söchting, M., Wieneke, S., 2023. A standardized catalogue of spectral indices to advance the use of remote sensing in Earth system research. Sci. Data 10, 197. https://doi.org/10.1038/s41597-023-02096-0

Nambiar, K.G., Morgenshtern, V.I., Hochreuther, P., Seehaus, T., Braun, M.H., 2022. A Self-Trained Model for Cloud, Shadow and Snow Detection in Sentinel-2 Images of Snow- and Ice-Covered Regions. Remote Sens. 14, 1825. https://doi.org/10.3390/rs14081825

Perich, G., Turkoglu, M.O., Graf, L.V., Wegner, J.D., Aasen, H., Walter, A., Liebisch, F., 2023. Pixel-based yield mapping and prediction from Sentinel-2 using spectral indices and neural networks. F. Crop. Res. 292, 108824. https://doi.org/10.1016/j.fcr.2023.108824

Qiu, S., Zhu, Z., He, B., 2019. Fmask 4.0: Improved cloud and cloud shadow detection in Landsats 4–8 and Sentinel-2 imagery. Remote Sens. Environ. 231, 111205. https://doi.org/10.1016/j.rse.2019.05.024

Raiyani, K., Gonçalves, T., Rato, L., Salgueiro, P., Marques da Silva, J.R., 2021. Sentinel-2 Image Scene Classification: A Comparison between Sen2Cor and a Machine Learning Approach. Remote Sens. 13, 300. https://doi.org/10.3390/rs13020300

Singh, G., Singh, S., Sethi, G., Sood, V., 2022. Deep Learning in the Mapping of Agricultural Land Use Using Sentinel-2 Satellite Data. Geographies 2, 691–700. https://doi.org/10.3390/geographies2040042

Sokolova, M., Lapalme, G., 2009. A systematic analysis of performance measures for classification tasks. Inf. Process. Manag. 45, 427–437. https://doi.org/10.1016/j.ipm.2009.03.002

Tarrio, K., Tang, X., Masek, J.G., Claverie, M., Ju, J., Qiu, S., Zhu, Z., Woodcock, C.E., 2020. Comparison of cloud detection algorithms for Sentinel-2 imagery. Sci. Remote Sens. 2, 100010. https://doi.org/10.1016/j.srs.2020.100010

WEI, L., HU, M., 2024. A review of medical ocular image segmentation. Virtual Real. Intell. Hardw. 6, 181–202. https://doi.org/10.1016/j.vrih.2024.04.001

Wright, N., Duncan, J.M.A., Callow, J.N., Thompson, S.E., George, R.J., 2024. CloudS2Mask: A novel deep learning approach for improved cloud and cloud shadow masking in Sentinel-2 imagery. Remote Sens. Environ. 306, 114122. https://doi.org/10.1016/j.rse.2024.114122

Zekoll, V., de los Reyes, R., Richter, R., 2022. A Newly Developed Algorithm for Cloud Shadow Detection—TIP Method. Remote Sens. 14, 2922. https://doi.org/10.3390/rs14122922

Zhang, Q., Yuan, Q., Li, J., Li, Z., Shen, H., Zhang, L., 2020. Thick cloud and cloud shadow removal in multitemporal imagery using progressively spatio-temporal patch group deep learning. ISPRS J. Photogramm. Remote Sens. 162, 148–160.

https://doi.org/10.1016/j.isprsjprs.2020.02.008
Zhang, Q., Yuan, Q., Li, Z., Sun, F., Zhang, L., 2021. Combined deep prior with low-rank tensor SVD for thick cloud removal in multitemporal images. ISPRS J. Photogramm. Remote Sens. 177, 161–173. https://doi.org/10.1016/j.isprsjprs.2021.04.021